

Fatigue behavior of Al_{0.5}CoCrCuFeNi high entropy alloys

M.A. Hemphill^a, T. Yuan^b, G.Y. Wang^a, J.W. Yeh^c, C.W. Tsai^c, A. Chuang^a, P.K. Liaw^{a,*}

^a Department of Materials Science and Engineering, University of Tennessee, Knoxville, TN, USA

^b Department of Industrial and Systems Engineering, Ohio University, Athens, OH, USA

^c Department of Materials Science and Engineering, National Tsing Hua University, Hsinchu 30013, Taiwan

Received 26 January 2012; received in revised form 6 June 2012; accepted 8 June 2012

Available online 23 August 2012

Abstract

Research was performed on an Al_{0.5}CoCrCuFeNi high entropy alloy (HEA) in an attempt to study the fatigue behavior. The present fatigue investigation shows encouraging fatigue resistance characteristics due to the prolonged fatigue lives of various samples at relatively high stresses. The current results indicate that the fatigue behavior of HEAs compares favorably with many conventional alloys, such as steels, titanium alloys, and advanced bulk metallic glasses with a fatigue endurance limit of between 540 and 945 MPa and a fatigue endurance limit to ultimate tensile strength ratio of between 0.402 and 0.703. Some unpredictability in the fatigue life of the samples was observed as scattering in the stress vs. lifetime plot. Weibull models were applied to predict the fatigue data and to characterize the variability seen in the HEAs. A Weibull mixture predictive model was used to separate the data into two, strong and weak, groups. This model predicts that at stresses above 858 MPa the median time to failure of specimens in the strong group will be greater than 10⁷ cycles. It was shown that microstructural defects, such as aluminum oxide inclusions and microcracks, may have a significant effect on the fatigue behavior of HEAs. It is believed that a reduction in the number of these defects may result in a fatigue behavior which exceeds that of conventional alloys.

© 2012 Acta Materialia Inc. Published by Elsevier Ltd. All rights reserved.

Keywords: Fatigue; High entropy alloy; Modeling

1. Introduction

Most practical alloy systems are based on a single principal element forming the matrix of the system with the addition of various elements to enhance particular properties of the material, such as iron- or copper-based alloys. This model greatly limits the number of viable systems and, thus, restricts the expanded use of alloying elements to obtain more desirable properties [1]. An alloy containing multiple principal elements is expected to yield many intermetallic compounds, with the possibility of complex microstructures with less desirable mechanical properties [2]. However, in high entropy alloys (HEAs) these phases are not prevalent, and solid solutions based on multiple principal elements are possible [2–4].

Thermodynamically, the tendency to form multi-element solid solution phases is likely using the Boltzmann hypothesis with the entropy of mixing ΔS_{Conf} given by Eq. (1):

$$\Delta S_{\text{Conf}} = -k \ln w = -R \ln \frac{1}{n} R \ln n \quad (1)$$

where k is Boltzmann's constant, w is the number of possible mixes, R is the gas constant, and n is the number of elements [2]. Because there are multiple principal elements they can be considered solute atoms. Elements with small atomic size differences are easily interchangeable and able to sit on lattice sites forming solid solutions. Moreover, the enthalpy of mixing of the elements does not favor the formation of compounds [3]. The resulting high entropy of mixing acts to lower the free energy of the solution phases. This trend is accompanied by sluggish diffusion due to the difficulty of cooperative migration of the various

* Corresponding author.

E-mail address: pliaw@utk.edu (P.K. Liaw).

elements. Thus, simple solid solutions and nanostructures that avoid the problems of difficult analyses and processing are formed [2,3].

Furthermore, it has been shown that the valence electron concentration (VEC) of the constituent elements has an effect on the phase stability [5]. Guo et al. have determined the face-centered cubic (fcc) and body-centered cubic (bcc) phase stabilities of solid solutions, such as HEAs, when the atomic size ratios are nearly identical [5]. This raises the possibility of thousands of alloy compositions [2] in addition to bulk metallic glass (BMG) HEA derivatives [6], an exciting development for future alloy design. HEAs can be defined as being composed of five or more elements in equimolar ratios or near equimolar ratios and can be extended to those compositions in which each principal element concentration is between 5 and 35 at.% [2]. These alloys could be used for a wide range of applications, such as those requiring high temperature strength, high tensile strength, increased wear resistance, and corrosion resistance [2,6–10].

This investigation will study the fatigue behavior of an $\text{Al}_{0.5}\text{CoCrCuFeNi}$ (molar ratio) HEA. Structural characterization of this alloy showed two distinct phases, a major α -fcc phase and a copper-rich β -fcc phase [11,12]. Both showed similar lattice constants of about 3.6 \AA [12]. In the homogenized and water-quenched condition both phases are in a supersaturated state and exhibit aging hardening between 300°C and 700°C due to the precipitation of Al- and Ni-rich bcc phases [13]. This precipitation hardening increases the strength but is accompanied by a loss of ductility. In the as-rolled and as-annealed (at 900°C) condition the $\text{Al}_{0.5}\text{CoCrCuFeNi}$ HEA displayed a better combination of strength and ductility compared with conventional alloys, such as 304 stainless steel and Ti-6Al-4V titanium alloys [13]. The mechanical properties of the as-cast $\text{Al}_x\text{CoCrCuFeNi}$ ($x = 0$ –3) alloys are readily available [14]. However, essentially no research has been conducted on investigating the fatigue behavior of this and other promising HEA systems [2–16]. The present research will examine and study the fatigue behavior of a $\text{Al}_{0.5}\text{CoCrCuFeNi}$ HEA. Moreover, statistical modeling will be conducted to further investigate the fatigue characteristics of the HEA.

2. Experimental procedures

2.1. Materials and sample preparation

The samples of $\text{Al}_{0.5}\text{CoCrCuFeNi}$ (molar ratio) were prepared by arc melting the constituent elements at a current of 500 A in a water-cooled copper hearth. The elements were all at least 99 wt.% pure, and melting was accomplished in a vacuum of at least 0.01 T. The melting and solidification processes were repeated at least five times to improve the chemical homogeneity of the sample. The cast samples were annealed at 1000°C for 6 h, water quenched, and cold rolled. The rolling reduction was

84%, with a final thickness of 3 mm. The rolled sheets were subsequently machined to fatigue samples with dimensions of $25 \times 3 \times 3$ mm for four point bending fatigue experiments, as described below. Samples were machined parallel to the rolling direction, i.e. the 25 mm length of the samples ran parallel to the rolling direction. Thus the applied stress on the tensile edge was parallel to the rolling direction. Two distinct microstructures were observed in this region (and in the samples as a whole) depending on the sample position in the mold during casting, as discussed below. Hence, the fatigue behavior as a function of the characteristic microstructure was also determined.

To remove as many surface imperfections as possible, the samples were polished on a Buehler rotating grinder and polisher. 240, 400, 600, and 1200 grits were used in that order. The sample was turned through 90° after each polishing step, finishing with the 1200 grit running parallel along the length direction of the sample.

2.2. Tensile test

Tensile experiments were performed on samples of the as-rolled HEAs to characterize the mechanical behavior of the alloys, and their results were used for comparison with other conventional alloys. The gage section of the specimens was machined to a size of 3×12 mm and tested in an Instron 4505 at a strain rate of $1 \times 10^{-3} \text{ s}^{-1}$. The specimens were tested to failure to determine the yield strength, ultimate tensile strength (UTS), and percent elongation.

2.3. Four point bending fatigue experiments

To study the fatigue behavior of the HEA samples four point bending tests were conducted at various applied loads and run until failure of the specimen or 10^7 cycles had been reached. The results of the fatigue tests were plotted as a typical stress range vs. number of cycles to failure ($S-N$) curve. The maximum stress σ on the tensile surface within the span of the two outer pins in the four point bending fatigue experiment was calculated, using the beam theory relationship [17]

$$\sigma = \frac{3P(S_o - S_i)}{2BW^2} \quad (2)$$

where P is the applied load, S_o is the outer span length 20 mm, S_i is the inner span length 10 mm, B is the thickness, and W is the height. In this investigation, $B = W = 3$ mm. The samples were tested at 10 Hz with a loading ratio of $R = \sigma_{\min}/\sigma_{\max} = 0.1$ [17], where σ_{\min} and σ_{\max} are the minimum and maximum applied stresses, respectively.

2.4. Microstructural characterization

High energy X-ray diffraction (XRD) was performed at the Advanced Photon Source (APS) using the 11-ID beam-

line located at the Argonne National Laboratory to obtain diffraction patterns of the sample for structural characterizations. The specimens were 1 mm thick using a beam energy of 115.27 keV. The scattered, transmitted X-rays were collected using a Mar345 image plate [18].

Microstructural features of the tensile regions of the fatigue samples were analyzed, using back-scattered electron microscopy (BSE), to determine the homogeneity of the microstructures. The fracture surfaces were investigated to study the fatigue mechanisms using scanning electron microscopy (SEM). The BSE, SEM, and energy-dispersive X-ray spectroscopy (EDS) analyses for the microstructural characterization were performed with a Gemini Leo 1525 scanning electron microscope at 15 and 20 keV.

3. Experimental results

3.1. Tension properties

Tension tests were initially performed on the samples to characterize the mechanical behavior of the rolled material. The results are shown in Fig. 1. The specimens exhibited a high yield stress of 1284 MPa and a UTS of, generally, 1344 MPa, exceeding that of conventional alloys, such as steels, titanium, aluminum, and nickel alloys [19–22]. Advanced alloys, such as BMGs, usually have higher strengths and lack tensile ductility. However, the present HEAs show the degree of plastic deformation necessary in structural applications with a tensile elongation of 7.6% for the as-rolled material (Fig. 1).

3.2. Microstructural characterization

Microstructural characterization was performed using synchrotron XRD and SEM. Fig. 2 shows a synchrotron XRD pattern of the Al_{0.5}CoCrCuFeNi HEA and averaged at azimuthal angles (ϕ) between 55° and 65°. The pattern indicates an fcc structure with the presence of some ordered structure indicated by the 100 peak. This ordered structure is the L₁₂ phase, similar to the Ni₃Al intermetallic compound homogeneously dispersed in a fcc matrix, as

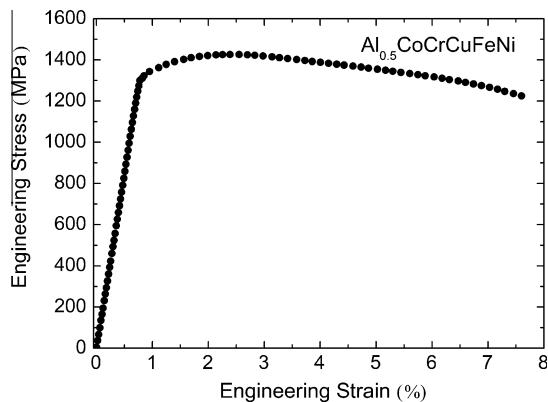


Fig. 1. Tension test flow curve for the Al_{0.5}CoCrCuFeNi HEA.

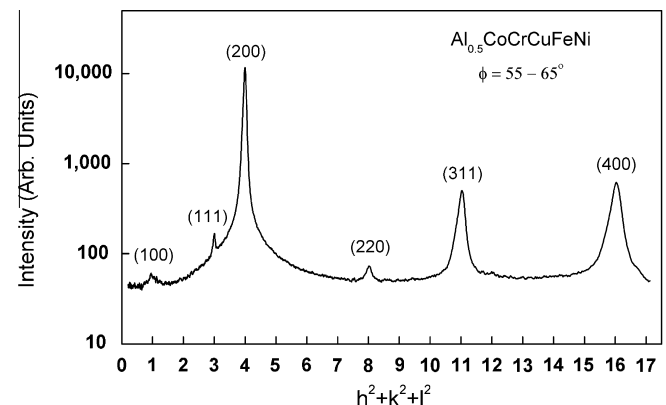


Fig. 2. Diffraction pattern of the Al_{0.5}CoCrCuFeNi HEA specimen using synchrotron high energy X-rays.

observed previously by transmission electron microscopy (TEM) [12,23]. The low peak intensity can be partially attributed to the high lattice strain present in the alloy [12]. The lower heights of the (1 1 1) and (2 2 0) peaks relative to the (2 0 0), (3 1 1), and (4 0 0) peaks are due to the texture in the sample, introduced by rolling deformation. The detection limits of XRD, approximately 1 vol.%, masked the detection of any minor phases, such as oxide particles, later shown to be present by EDS analysis. Only one set of fcc peaks is seen in the XRD pattern. Previous studies have shown that the lattice constants of these two phases are very similar, approximately 3.6 Å [12]. This trend will cause an overlap of the characteristic diffraction peaks, if the resolution of the experimental set-up is not high enough. It is important to note that because no bcc characteristic peaks were observed the structure is indeed a two-phase fcc structure.

BSE and EDS analyses of the specimens were performed to observe and determine the elemental compositions of the specimens. Fig. 3 shows an SEM micrograph of a typical sample. The microstructure consists of two phases: the α -fcc matrix phase, formed from the fcc dendrite phase (the

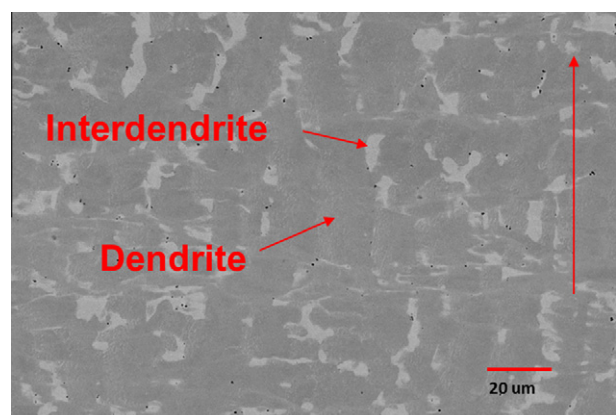


Fig. 3. SEM micrograph showing the α -fcc matrix dendrite phase and β -Cu-rich fcc interdendritic phase elongated along the rolling direction, indicated by the arrow.

dark phase), and the β -fcc Cu-rich phase (the light phase), developed from the fcc Cu-rich interdendritic phase. The Cu-rich phase is seen to elongate along the rolling direction [13]. The elemental compositions of these two phases are shown in Table 1. It can be observed that the Cu-rich phase has a Cu content of 59 at.%. This phase separation is due to the relatively large positive bonding energies of Cu–Fe, Cu–Co, and Cu–Cr due to the tendency of copper to segregate into clusters [12,23].

3.3. Four point bending fatigue

Four point bending fatigue tests were performed and the results plotted as the stress range (the maximum stress calculated from Eq. (2) and the range ($0.9\sigma_{\max}$) determined using $R = 0.1$) vs. the number of cycles to failure or 10^7 cycles to give the S–N curve seen in Fig. 4. There is a noticeable amount of scatter at various stress levels. The results display the typical fatigue behavior for crystalline materials of an increase in the number of cycles to failure as the stress level decreases. At a maximum stress of 1250 MPa, near the yield stress of 1284 MPa, most failures were within an order of magnitude of 35,000–450,000 cycles, although there was still a wide range of scatter. As the stress level decreased the spread in the data became even more pronounced, which is generally characteristic of fatigue behavior [24]. Estimations of the endurance limits based on the stress ranges were within a lower bound of 540 MPa and an upper bound of 945 MPa. Values were chosen because the specimens reached 10^7 cycles without failure.

The microstructural morphology was taken into account to try to determine whether this feature had an effect on the fatigue life. Although the fatigue specimens were machined parallel to the rolling direction, the morphologies of the matrix phase (α) and the Cu-rich phase (β) in the tensile region of the sample might be different from sample to sample. This trend could be tracked to their position and different heat flow directions in the copper mold during solidification. Therefore, the orientation of the loading direction in relation to the different morphologies was investigated. The SEM micrographs presented in Fig. 5 show two typical morphologies observed in the tensile region of the samples. Fig. 5a displays a parallel morphology, which features a lamellar flow pattern of alternating α and β phases. Fig. 5b presents a vertical type characterized by a random orientation of the α and β phases. After microstructure identification for all tested samples by

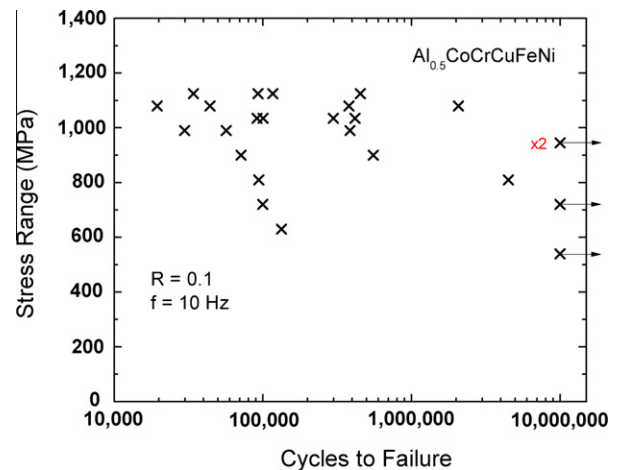


Fig. 4. S–N curve for the $\text{Al}_{0.5}\text{CoCrCuFeNi}$ HEA plotted as the stress range vs. the number of cycles to failure.

SEM, Fig. 4 was replotted as Fig. 6, showing the fatigue behavior of the parallel and vertical types of samples. It appears that there is no correlation between the scatter in the fatigue life and the orientation of the loading direction with respect to the different morphologies, and later statistical modeling efforts confirmed this trend. Thus the orientation and morphology of the phases do not appear to have a significant effect on the fatigue life.

A likely cause of the variable fatigue life is the number of defects in the sample, introduced during the casting and rolling processes, in particular aluminum oxide-rich particles formed during the melting and solidification process. EDS analyses were performed on these particles to examine their approximate compositions (Fig. 7). This feature shows the presence of approximately 50% oxygen, consistent with aluminum oxide particles. These particles provide nucleation sites for microcracks, due to stress concentration at the particles.

Fig. 8 presents the number of cycles to failure vs. the number of defects per $240 \times 165 \mu\text{m}$ unit area observed at $500\times$ magnification in specimens at various stress levels. It can be observed that a decrease in the number of defects generally correlates with an increase in the fatigue life at various stress levels. In reality the air-cooled and final solidification sides of the casting contain greater segregation, more inclusions, and more shrinkage pores, which could induce microcracks during cold rolling. If high densities of these microcracks are located on the tensile side during four point fatigue loading then the fatigue resistance will be reduced, and failure would occur after fewer cycles.

3.4. Fractography

Fracture surfaces were analyzed to determine the unique fatigue characteristics of the samples, such as crack initiation sites, crack propagation, and final fracture. Fig. 9a shows the fracture surface of a sample that failed at a stress of 900 MPa after 555,235 cycles. Fig. 9b presents the crack

Table 1
EDS analyses of the matrix and Cu-rich phases in the $\text{Al}_{0.5}\text{CoCrCuFeNi}$ HEA microstructures.

Al _{0.5} CoCrCuFeNi phase compositions (at.%)						
Region	Al	Co	Cr	Cu	Ni	
Matrix phase	7	20	21	11	22	18
Cu-rich phase	10	5	4	59	6	15

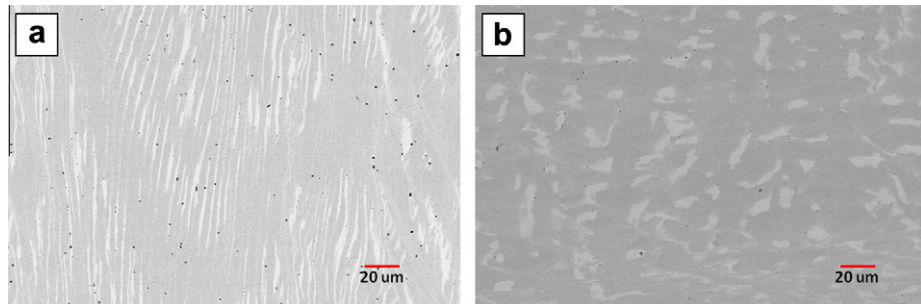


Fig. 5. SEM micrographs showing two different types of morphology: (a) the parallel type with a lamellar flow pattern of alternating α and β phases and (b) the vertical type with a random orientation of α and β phases.

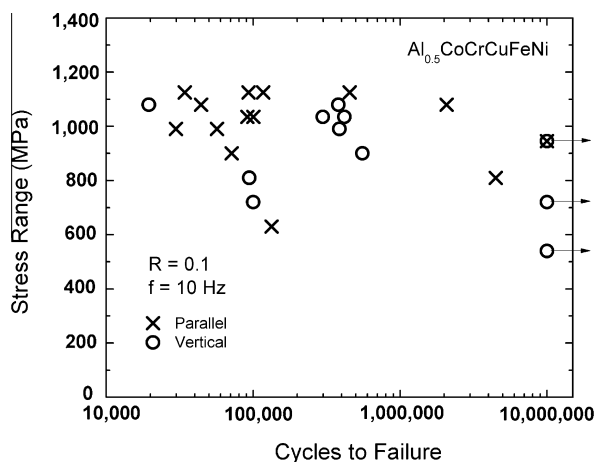


Fig. 6. $S-N$ curves for the $\text{Al}_{0.5}\text{CoCrCuFeNi}$ HEAs showing scattering of the cycles to failure for the parallel and vertical type morphologies, respectively, in the samples.

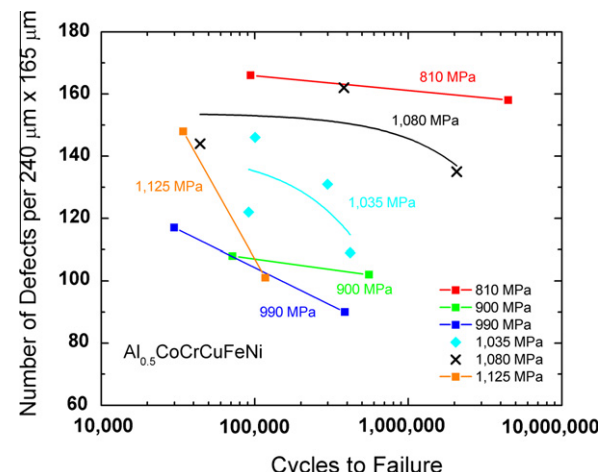


Fig. 8. The cycles to failure compared with the number of surface defects at various stress levels showing that as the number of defects decreases the life generally increases at a particular maximum stress level.

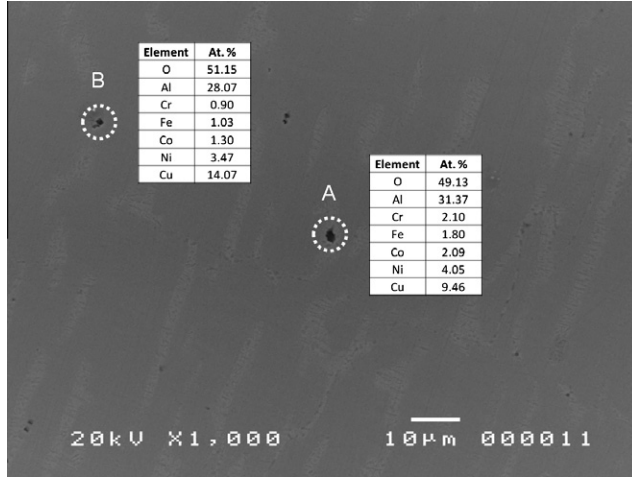


Fig. 7. SEM micrograph with EDS analyses of the aluminum oxide particles. The compositions of the regions labeled A and B are given in the corresponding tables, indicating the presence of aluminum oxide particles.

initiation behavior from microcracks that formed from defects on the surface of the sample. The samples exhibited similar fracture patterns, with crack initiation within the tensile region of the sample surface. Cracks usually

initiated at defects present on the surface, as discussed below, or at the corner of the samples. These areas represent high stress concentration regions favorable for crack nucleation. Numerous cracks nucleated and grew perpendicular to the stress in the specimen (parallel to the applied load) through the tensile region. Crack propagation generally occurred through approximately one-third of the cross-section before final failure, depending on the applied stress level. Fig. 10 presents SEM micrographs of the various regions of the fracture surface showing the typical fatigue characteristics of striations in the crack propagation region (Fig. 10a) and dimples in the final failure region, indicating a ductile fracture mechanism (Fig. 10b).

4. Predictive models for fatigue life

4.1. Weibull predictive model

The phenomenon of fatigue shows a stochastic nature [25]. Statistical models and data analysis methods are, therefore, necessary tools in studying fatigue behavior. In this investigation statistical fatigue-lifespan models were developed to predict the fatigue life of the HEAs. The first

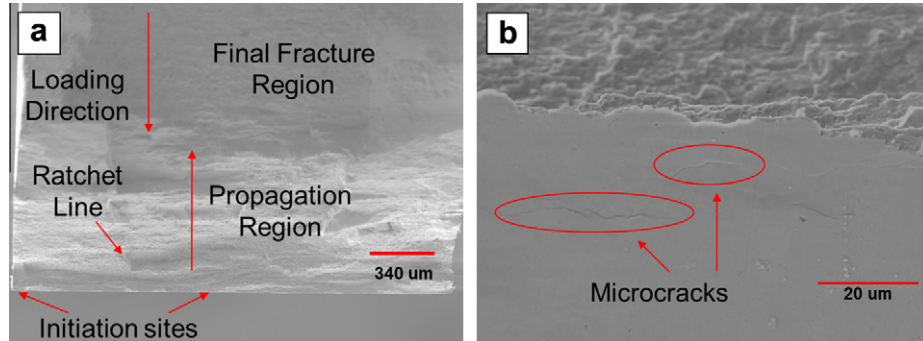


Fig. 9. (a) SEM micrograph of the fracture surface of a sample that failed at a stress value of 900 MPa after 555,235 cycles. (b) Crack initiation occurred at the surface of the sample, with microcracks forming before the fatigue test. Note that the loading direction comes out of the page.

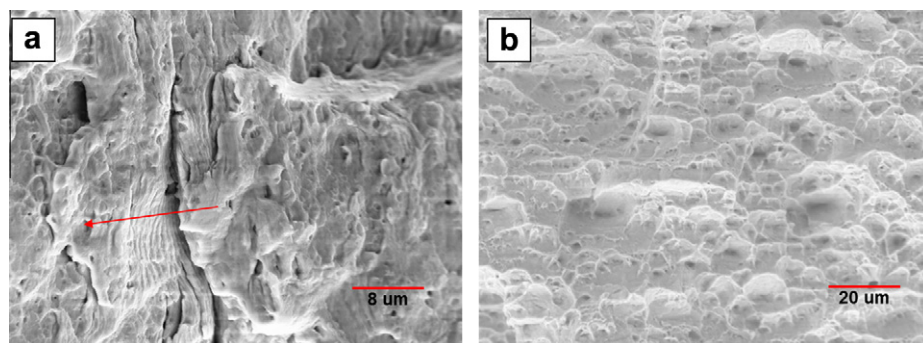


Fig. 10. SEM micrographs showing (a) fatigue striations in the crack propagation region with the crack growth direction indicated by the arrow and (b) dimples in the final fracture region, indicating ductile fracture of the sample.

predictive model assumes a Weibull distribution to describe the fatigue–lifespan distribution in each fixed stress range, based on a commonly used analytical representation of the S – N curve given by Eq. (3) [26]

$$N(S) = cS^{-d}, \quad (3)$$

where S denotes the applied stress range, $N(S)$ is the expected number of fatigue life cycles at stress level S , and c and d are positive material parameters. Taking the natural logarithm on the S – N relation (Eq. (3)) results in

$$\log(N(S)) = \gamma_0 + \gamma_1 \log(S), \quad (4)$$

where $\gamma_0 = \log(c)$ and $\gamma_1 = -d$. The S – N relation given by Eqs. (3) and (4) provides a simple way to relate the effect of a stress applied to the test item to the number of cycles to fatigue failure [26]. However, it does not capture the variability in the observed fatigue–lifespan data. To account for such variability we introduced an error term ε into Eq. (4), i.e.

$$\log(N(S)) = \gamma_0 + \gamma_1 \log(S) + \varepsilon. \quad (5)$$

We assume that the error term ε follows the standardized smallest extreme value distribution. The fatigue–lifespan model given by Eq. (5) then becomes a Weibull regression model [27]. The Weibull regression model given by Eq. (5) can be written as an equivalent Weibull-accelerated life testing model that is widely used in reliability engineering and lifetime data analyses [27]. The fatigue life at a

given stress level S follows the Weibull distribution. The probability density function (pdf) and the cumulative distribution function of the Weibull distribution are described by Eqs. (6) and (7), respectively:

$$f(N(S)|\alpha(S), \beta) = \frac{\beta}{\alpha(S)} \left(\frac{N(S)}{\alpha(S)} \right)^{\beta-1} \exp \left(- \left(\frac{N(S)}{\alpha(S)} \right)^\beta \right) \quad (6)$$

$$F(N(S)|\alpha(S), \beta) = 1 - \exp \left(- \left(\frac{N(S)}{\alpha(S)} \right)^\beta \right) \quad (7)$$

where β is the Weibull shape parameter, and the Weibull scale parameter $\alpha(S)$ depends on the stress S according to, $\log(\alpha(S)) = \gamma_0 + \gamma_1 \log(S)$. (8)

In this experiment four samples had not failed when the bending fatigue test was terminated at 10^7 cycles, and they became censored observations. The probability of obtaining a censored observation at stress level S is given by Eq. (9):

$$P(N(S) \geq N_c) = 1 - F(N_c|\alpha(S), \beta) = \exp \left(- \left(\frac{N_c}{\alpha(S)} \right)^\beta \right), \quad (9)$$

where N_c equals 10^7 cycles, denoting the censor time of the experiment.

The first fatigue–lifespan model, hereafter termed the Weibull predictive model, consists of two components:

the Weibull distribution describing the fatigue–lifespan variability at a fixed stress range, and the relation describing the stress dependence of the fatigue life, given by Eq. (8). Note that lifetime distributions other than the Weibull distribution may be used. For example, if the error term ε in Eq. (5) is assumed to be a standardized normal random variable, then the fatigue life $N(S)$ at a given stress level S follows a log–normal distribution. This study assumes a Weibull distribution, because it is the most widely used lifetime distribution in reliability engineering and lifetime data analyses, and has been applied to model the fatigue behavior of a variety of materials, such as steels [28,29], aluminum alloys [30], and metallic glasses [31,32].

The Weibull predictive model has three unknown model parameters, β , γ_0 , and γ_1 , which can be estimated by the maximum likelihood method [27]. We denote the observed fatigue–lifespan data by $\{(N_i, S_i, \delta_i), i = 1, 2, \dots, m\}$, where m is the total number of samples tested, and N_i and S_i are, respectively, the fatigue–lifespan cycles and the applied stress to the i th sample. The binary indicator variable δ_i equals 1 if N_i is a failure observation, and $\delta_i = 0$ if N_i is a censored observation. Given the observed fatigue–lifespan data the maximum likelihood method estimates the model parameters by maximizing the likelihood function given in Eq. (10)

$$L(\beta, \gamma_0, \gamma_1) = \prod_{i=1}^m \left[\frac{\beta}{e^{\gamma_0 + \gamma_1 \log(S_i)}} \left(\frac{N_i}{e^{\gamma_0 + \gamma_1 \log(S_i)}} \right)^{\beta-1} \right]^{\delta_i} \times \exp \left[-\left(\frac{N_i}{e^{\gamma_0 + \gamma_1 \log(S_i)}} \right)^{\beta} \right]. \quad (10)$$

Once the model parameters are estimated the fatigue–lifespan behavior at a given stress S can be predicted by estimating the p quantile life, which is given by (Eq. (11)),

$$N_p(S) = \exp(\gamma_0 + \gamma_1 \log(S))(-\log(1-p))^{1/\beta}. \quad (11)$$

The median fatigue life (i.e. $p = 0.5$) can be used to describe the relationship between the applied stress and the average fatigue–lifespan response. The 2.5 and 97.5 quantiles can be employed to construct a 95% predictive interval for the fatigue life, and to quantify the scatter in the fatigue life cycles.

4.2. Weibull mixture predictive model

The Weibull predictive model, however, may not be able to adequately characterize the excessive variability in the observed fatigue data shown in Fig. 4. The observed fatigue lives seem to form two groups, a strong group and a weak group, especially when the applied stress was less than 1000 MPa. The fatigue lives in the weak group were much shorter than those in the strong group. This variability in the fatigue data may be caused by variability in the defect density in the experimental units, as discussed below. A Weibull mixture model (termed the multimodal Weibull model) may be used when the population of units is

non-homogeneous [33]. The second predictive model therefore assumes a mixture of two Weibull distributions for the fatigue lives at each stress range value. The pdf and cdf of the Weibull mixture model are given in Eqs. (12) and (13), respectively,

$$f(N(S)|p, \alpha_w(S), \beta_w, \alpha_s(S), \beta_s) = p \frac{\beta_w}{\alpha_w(S)} \left(\frac{N(S)}{\alpha_w(S)} \right)^{\beta_w-1} \exp \left(-\left(\frac{N(S)}{\alpha_w(S)} \right)^{\beta_w} \right) + (1-p) \frac{\beta_s}{\alpha_s(S)} \left(\frac{N(S)}{\alpha_s(S)} \right)^{\beta_s-1} \exp \left(-\left(\frac{N(S)}{\alpha_s(S)} \right)^{\beta_s} \right), \quad (12)$$

$$F(N(S)|p, \alpha_w(S), \beta_w, \alpha_s(S), \beta_s) = p \left[1 - \exp \left(-\left(\frac{N(S)}{\alpha_w(S)} \right)^{\beta_w} \right) \right] + (1-p) \left[1 - \exp \left(-\left(\frac{N(S)}{\alpha_s(S)} \right)^{\beta_s} \right) \right], \quad (13)$$

where the subscripts w and s denote the weak and strong groups, respectively, and the parameter p is the fraction of samples belonging to the weak group. The probability of obtaining a censored observation in the Weibull mixture model is then given by Eq. (14).

$$P(N(S) > N_c) = p \exp \left[-\left(\frac{t}{\alpha_w(S)} \right)^{\beta_w} \right] + (1-p) \exp \left[-\left(\frac{t}{\alpha_s(S)} \right)^{\beta_s} \right]. \quad (14)$$

Again, the Weibull scale parameters $\alpha_w(S)$ and $\alpha_s(S)$ are assumed to be dependent on the stress S according to Eqs. (15) and (16)

$$\log(\alpha_w(S)) = \gamma_{w,0} + \gamma_{w,1} \log(S), \quad (15)$$

and

$$\log(\alpha_s(S)) = \gamma_{s,0} + \gamma_{s,1} \log(S), \quad (16)$$

respectively. The second fatigue–lifespan model, termed the Weibull mixture predictive model, has 7 unknown parameters p , $\gamma_{w,0}$, $\gamma_{w,1}$, β_w , $\gamma_{s,0}$, $\gamma_{s,1}$, and β_s . The unknown parameters can again be estimated, using the maximum likelihood method. The likelihood function of the model parameters is given by:

$$L(p, \beta_w, \gamma_{w,0}, \gamma_{w,1}, \beta_s, \gamma_{s,0}, \gamma_{s,1}) = \prod_{i=1}^m f(N_i)^{\delta_i} (1 - F(N_i))^{1-\delta_i}, \quad (17)$$

where $f(N_i)$ and $F(N_i)$ are given by Eqs. (12) and (13), respectively. Once the maximum likelihood estimates of the seven model parameters are obtained the observed fatigue data can be clustered into the two groups. If N_i is a failure observation the likelihoods of the i th sample belonging to the weak group and the strong group are given by

$$\frac{\beta_w}{e^{\gamma_{w,0} + \gamma_{w,1} \log(S_i)}} \left(\frac{N_i}{e^{\gamma_{w,0} + \gamma_{w,1} \log(S_i)}} \right)^{\beta_w - 1} \exp \left(- \left(\frac{N_i}{e^{\gamma_{w,0} + \gamma_{w,1} \log(S_i)}} \right)^{\beta_w} \right)$$

and

$$\frac{\beta_s}{e^{\gamma_{s,0} + \gamma_{s,1} \log(S_i)}} \left(\frac{N_i}{e^{\gamma_{s,0} + \gamma_{s,1} \log(S_i)}} \right)^{\beta_s - 1} \exp \left(- \left(\frac{N_i}{e^{\gamma_{s,0} + \gamma_{s,1} \log(S_i)}} \right)^{\beta_s} \right),$$

respectively. The i th sample is then assigned to the group with a higher likelihood value. Similarly, if N_j is a censored observation the likelihoods of the j th sample belonging to the two groups are given by

$$\exp \left(- \left(\frac{N_j}{e^{\gamma_{w,0} + \gamma_{w,1} \log(S_j)}} \right)^{\beta_w} \right)$$

and

$$\exp \left(- \left(\frac{N_j}{e^{\gamma_{s,0} + \gamma_{s,1} \log(S_j)}} \right)^{\beta_s} \right),$$

respectively. The p quantile fatigue lives of the strong group and the weak group are predicted by Eqs. (18) and (19),

$$N_{p,w}(S) = \exp(\gamma_{w,0} + \gamma_{w,1} \log(S))(-\log(1-p))^{1/\beta_w}, \quad (18)$$

$$N_{p,s}(S) = \exp(\gamma_{s,0} + \gamma_{s,1} \log(S))(-\log(1-p))^{1/\beta_s}, \quad (19)$$

respectively.

4.3. General log-linear model

This study also developed a third predictive model to study the correlation between the fatigue life and the type of morphology. A binary variable X_i was introduced to indicate the morphology type of the i th experimental unit, i.e. $X_i = 0$ for the parallel morphology, $X_i = 1$ for the vertical morphology. A general log-linear model is assumed to describe the effect of stress and morphology on the Weibull scale parameter, i.e.

$$\ln \alpha_i = \gamma_0 + \gamma_1 \log(S_i) + \gamma_2 X_i. \quad (20)$$

To determine whether the morphology affects the fatigue life, a test of significance can be performed on the regression coefficient γ_2 . The two hypotheses in the test of significance are $H_0: \gamma_2 = 0$ vs. $H_1: \gamma_2 \neq 0$. If H_0 is rejected there is evidence that the type of morphology affects the fatigue life. If the test of significance fails to reject H_0 there is no evidence against the hypothesis that the morphology does not affect the fatigue life.

5. Computational results and implications

5.1. Weibull predictive model

The Weibull predictive model is first applied to analyze the observed fatigue-lifespan data. The maximum likelihood estimates of the three model parameters are

$\beta = 0.492$, $\gamma_0 = 70.869$, and $\gamma_1 = -8.327$. Fig. 11 shows the predicted median, 0.025 quantile, and 0.975 quantile fatigue lives. The 2.5 and 97.5 quantiles are used to construct the 95% predictive interval for the fatigue life. This 95% predictive interval captures all the failure observations. This predictive interval, however, is very wide, due to the excessive variability in the data and the limited sample size.

5.2. Weibull mixture model

Next, the Weibull mixture predictive model is used to analyze the experimental data. The maximum likelihood estimates of the seven model parameters are $p = 0.369$, $\beta_w = 3.773$, $\gamma_{w,0} = 15.238$, $\gamma_{w,1} = -0.555$, $\beta_s = 0.612$, $\gamma_{s,0} = 126.454$, and $\gamma_{s,1} = -16.245$. Fig. 12 shows the quantile lives predicted by the Weibull mixture predictive model. The observed data are also clustered into two groups. We are more interested in the strong group, because samples in the strong group contain fewer fabrication defects and can, therefore, reveal the intrinsic fatigue behavior of the HEA, as discussed below. The median life of the strong group exceeded 10^7 cycles when the applied stress was less than 858 MPa, which may be used as an estimate of the endurance limit of this HEA.

5.3. Comparison of the Weibull predictive model and Weibull mixture predictive model

When the applied stresses were 1125, 1080, and 1035 MPa there were four failure observations at each of the three stress levels. A Kolmogorov-Smirnov goodness of fit test was conducted to check whether the Weibull distribution or the Weibull mixture distribution are appropriate for the fatigue-lifespan data observed at these three stress levels. Table 2 summarizes the Kolmogorov-Smirnov test statistic values. Because all the test statistic values are less than the critical value of 0.494 [34] there is no evidence to reject the Weibull or the Weibull mixture model as

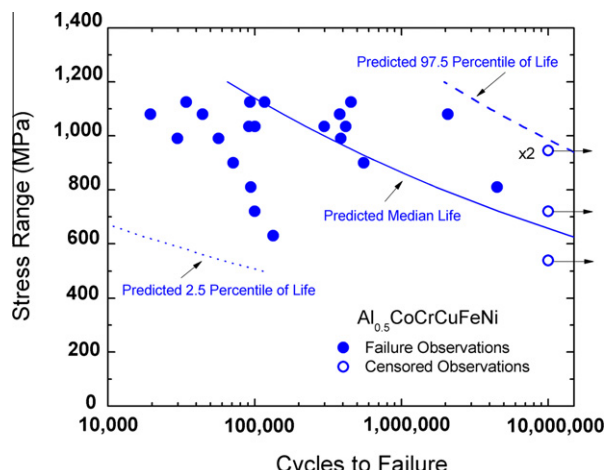


Fig. 11. Predicted quantile lives using the Weibull predictive model.

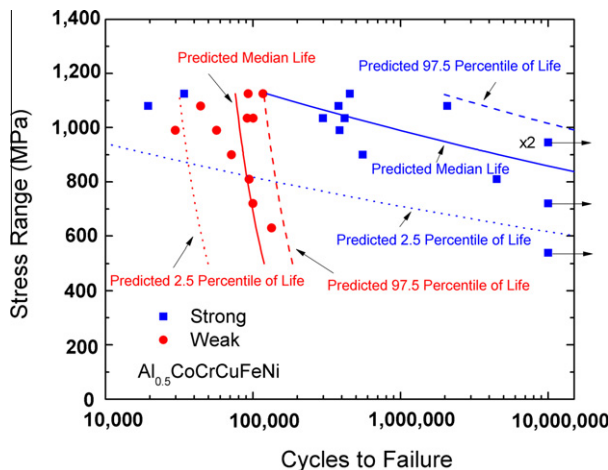


Fig. 12. Predicted quantile lives using the Weibull mixture predictive model. Squares, observations of the weak group; circles, observations of the strong group.

Table 2

Kolmogorov-Smirnov goodness of fit test for the Weibull and the Weibull mixture distributions.

Stress range (MPa)	Kolmogorov-Smirnov test statistics	
	Weibull distribution	Weibull mixture distribution
1125	0.32	0.31
1080	0.22	0.33
1035	0.39	0.39

an appropriate model for the data collected at these three stress levels. A goodness of fit test was not conducted for the fatigue data collected at other stress levels because of the very small sample sizes.

To determine which predictive model is better for the observed data we applied three commonly used model selection criteria, i.e. the log-likelihood, the Akaike information criterion (AIC), and the Bayesian information criterion (BIC). The AIC and BIC are defined by Eqs. (21) and (22), respectively,

$$AIC = 2 \log L - 2k, \quad (21)$$

$$BIC = 2 \log L - k \log m, \quad (22)$$

where $\log L$, n , and k are the log-likelihood, the number of observations, and the number of parameters in the model, respectively. The log-likelihood measures how well a model fits the data. Using more complex models usually provides a better fit to the data. The AIC and the BIC, however, adversely affect the complexity of the model, where

complexity refers to the number of parameters in the model. A model with a higher $\log L$, AIC, or BIC value is usually preferred. Table 3 lists the three model selection criteria for the two predictive models. All three criteria indicate that the Weibull mixture predictive model is preferred over the Weibull predictive model.

5.4. Morphology effect on fatigue life

It was thought that the microstructure, specifically the orientation of the α and β phases due to casting, could play an important role in affecting the fatigue characteristics. To study the relationship between the fatigue life and the morphology the third predictive model was applied to analyze the observed fatigue-lifespan data for the strong group. The Weibull distribution was used to model the variability in fatigue life at a fixed stress level for the strong group, and the Weibull scale parameter was modeled by the general log-linear relation (Eq. (20)). The test of significance for the regression coefficient γ_2 yielded a P value of 0.18. Hence the test fails to reject $H_0: \gamma_2 = 0$ at the commonly used significance levels of 0.05 and 0.10. Analysis of the observations for the weak group results in the same conclusion, with a P value of 0.73. Therefore, there is no evidence to indicate that morphology affects the fatigue life.

6. Discussion

Both the experimental (Fig. 8) and computational (Fig. 12) results confirm that the fatigue-lifecycle relations of the HEA are mainly controlled by defects. Fig. 13 shows that the strong group tends to have fewer defects on average than the weak group. At a given stress level the strong samples with fewer defects tend to exhibit longer fatigue lives than the weak samples with more defects. Therefore, the control of defects during the fabrication processes is critically important for the future advancement and application of HEAs. It is believed that a reduction in the number of defects could result in a more favorable fatigue behavior compared with that of conventional alloys.

In total, four specimens reached the endurance limit, at stresses of 540 and 720 MPa and two specimens at 945 MPa (Fig. 4). These values correspond to excellent fatigue ratios (equal to a fatigue endurance limit/UTS) between 0.402 and 0.703, respectively. The fatigue endurance limit estimated by the Weibull mixture predictive model was 858 MPa for the strong group, which corresponds to a fatigue ratio of 0.638. These estimates show that HEAs have favorable and/or greater endurance limits

Table 3
Model selection between the Weibull predictive model and the Weibull mixture predictive model.

Model	Model-selection criteria		
	Log-likelihood, $\log L$	$AIC = 2 \log L - 2k$	$BIC = 2 \log L - k \log m$
Weibull	-303.9	-613.7	-617.4
Weibull mixture	-293	-601.9	-610.5

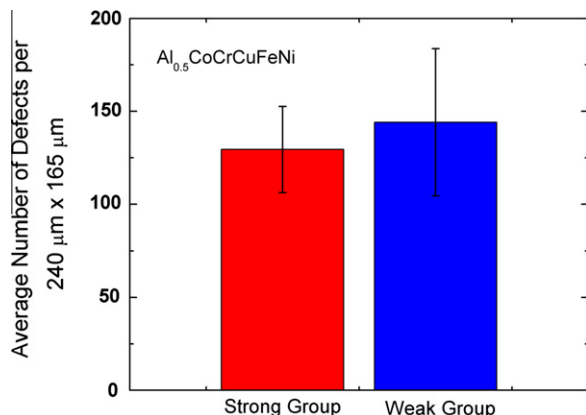


Fig. 13. Bar graph of the average number of defects observed for the weak and strong groups. The weak group tends to have more defects than the strong group, which can lead to shorter fatigue lifetimes.

and fatigue ratios comparable with steels, aluminum alloys, nickel alloys, titanium alloys, and BMGs, as shown in Fig. 14 and Table 4 [17,19–22] and detailed below.

Fig. 14a presents HEAs with a lower bound endurance limit comparable with 15-5PH stainless steel, 4340 steel, and titanium alloys, and an upper bound surpassed only

by some BMGs. This trend is due to the extremely high UTS of BMGs (~1900 MPa) relative to HEAs (1344 MPa). Fig. 15a illustrates this relationship comparing the fatigue-endurance limit vs. UTS. One reason for the high fatigue strengths of HEAs is the high tensile strength of these materials. It can be clearly seen that as the UTS increases the endurance limit will also increase in a linear fashion, approximately equal to 0.5 for most materials [21]. HEAs follow a similar pattern and even exceed this ratio, with an upper bound of 0.703 (Figs. 14b and 15b, and Table 4).

To better compare the fatigue performance of HEAs with other materials with respect to their UTS the fatigue ratios are used, as shown in Figs. 14b and 15b, and Table 4. The lower bound of the fatigue ratios of HEAs compares favorably with those of steels, titanium, and nickel alloys, and outperforms zirconium alloys, as well as some Zr-based BMGs. Moreover, for some materials, such as ultra-high strength steels and wrought aluminum alloys, their high tensile strengths result in lower fatigue ratios due to their brittle nature [21]. The strong group of HEAs tends to outperform these materials by displaying a greater fatigue ratio than materials with comparable tensile

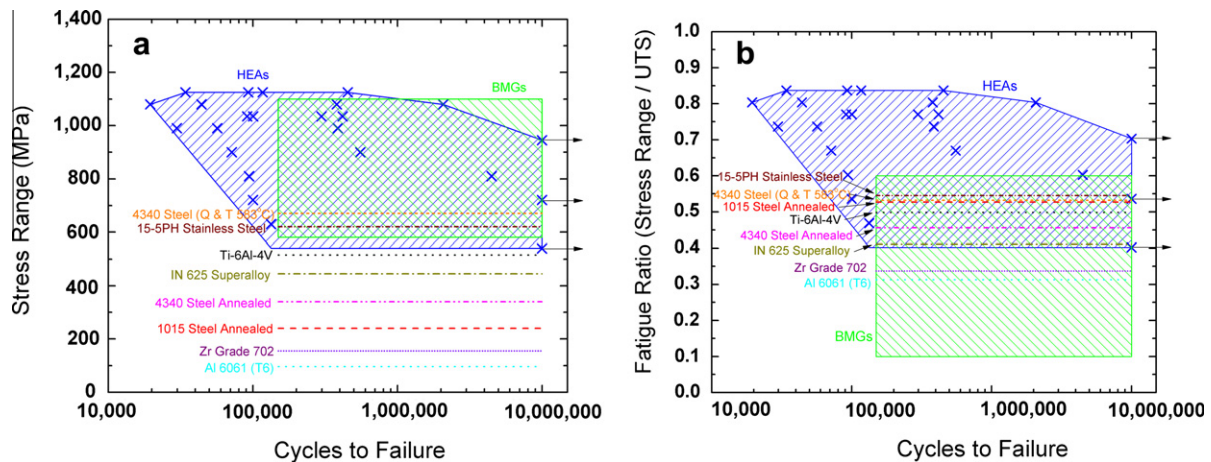


Fig. 14. $S-N$ curves comparing (a) the endurance limits and (b) the fatigue ratios of the $\text{Al}_{0.5}\text{CoCrCuFeNi}$ HEA, other conventional alloys, and BMGs [17,19–22].

Table 4

Comparison of the fatigue endurance limits, ultimate strengths, and fatigue ratios (EL/UTS) of the $\text{Al}_{0.5}\text{CoCrCuFeNi}$ HEA with various other alloys [17,19,20,22].

Material	Ultimate tensile strength (MPa)	Fatigue endurance limit (MPa)	Fatigue ratio
HEA $\text{Al}_{0.5}\text{CoCrCuFeNi}$ [this study]	1344	540/945	0.402/0.703
4340 Steel (Quenched & tempered 538 °C) [20]	1260	670	0.532
4340 steel annealed [20]	745	340	0.456
15–5PH stainless steel [20]	1137	620	0.545
1015 steel annealed [20]	455	240	0.527
Ti-6Al-4V [20]	1035	515	0.498
IN 625 superalloy [20]	1082	445	0.411
Al 6061 (T6) [20]	310	96	0.313
Zr grade 702 [22]	430	155	0.36
Zr-based BMGs [17,19]	1480–1900	239–983	0.161–0.517

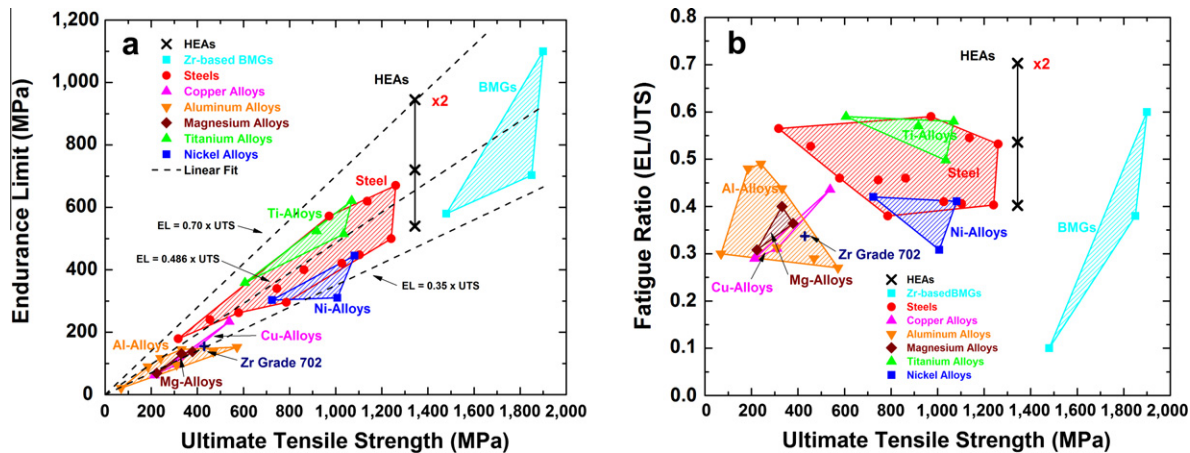


Fig. 15. Plots comparing (a) the endurance limits and (b) the fatigue ratios of the Al_{0.5}CoCrCuFeNi HEA as a function of the UTS of other structural materials and BMGs [17,19–22].

strengths due to the reduced number of defects. The upper bound of the fatigue limit of HEAs is significantly higher than that of other conventional alloys and BMGs, showing that HEAs have the potential to outperform these materials in structural applications with improved fabrication and processing.

These results are very encouraging for future research, exhibiting the potential for excellent fatigue resistance in HEAs, with possible long fatigue lives, even at stresses approaching the ultimate stress. Because of the lack of literature on the fatigue behavior of HEAs the focus of continuing research should be placed on the data points that show an unexpectedly long fatigue life. If the necessary information on fatigue resistance can be obtained, along with the development of a prediction model for fatigue specimens, HEAs have a promising future in numerous applications as components in high fatigue environments.

7. Conclusions

The fatigue studies show encouraging fatigue resistance characteristics due to the long fatigue lives of various samples at relatively high stresses. The fatigue endurance limit was found to be between 540 and 945 MPa. Some scattering of the fatigue life was seen in the S-N curves. A possible explanation of the scatter could be the different defect densities of aluminum oxide particles and microcracks introduced during the casting and rolling operations. The Weibull mixture predictive model showed two main groups, with the strong group having a predicted median time to failure of greater than 10⁷ at 858 MPa. The fatigue endurance limit to UTS ratio of between 0.402 and 0.703 compares favorably with conventional materials, such as steels, and nickel, aluminum, and titanium alloys, and advanced BMGs. This trend may be partially due to the high tensile strength of HEAs, compared with these other materials. However, when the fatigue ratios of these materials are compared HEAs may surpass conventional alloys, with a reduction in defects introduced during fabrication

and processing. Al_{0.5}CoCrCuFeNi HEAs show promising fatigue resistance characteristics and may be useful in future applications where fatigue is a factor. More studies need to be conducted to further investigate the fatigue behavior as well as prediction models for HEAs.

Acknowledgements

The authors would like to acknowledge financial support from the National Science Foundation (NSF) under programs DMR-0909037, CMMI-0900271, and CMMI-1100080 with Dr A. Ardell and Dr C.V. Cooper, respectively, serving as program directors, and the US Department of Energy Office of Nuclear Energy's Nuclear Energy University Programs (NEUP) under contract number 00119262 with Dr R.O. Jensen Jr as program manager.

References

- [1] Davis JR, editor. Metals handbook, vol. 1, 10th ed. Metals Park (OH): ASM International; 1990.
- [2] Yeh JW, Chen SK, Lin SJ, Gan JY, Chin TS, Shun TT, et al. Adv Eng Mater 2004;6:299.
- [3] Zhang Y, Zhou YJ, Lin JP, Chen GL, Liaw PK. Adv Eng Mater 2008;10:534.
- [4] Zhou YJ, Zhang Y, Wang YL, Chen GL. Mater Sci Eng A 2007;454:260.
- [5] Takeuchi A, Chen N, Wada T, Yokoyama Y, Kato H, Inoue A, et al. Intermetallics 2011;19:1545.
- [6] Guo S, Ng C, Lu J, Liu CT. J Appl Phys 2011;109:103505.
- [7] Senkov ON, Wilks GB, Miracle DB, Chuang CP, Liaw PK. Intermetallics 2010;18:1758.
- [8] Senkov ON, Wilks GB, Scott JM, Miracle DB. Intermetallics 2011;19:698.
- [9] Senkov ON, Scott JM, Senkova SV, Miracle DB, Woodward CF. J Alloys Compd 2011;509:6043.
- [10] Chuang MH, Tsai MH, Wang WR, Lin SJ, Yeh JW. Acta Mater 2011;59:6308.
- [11] Liu ZY, Guo S, Liu XJ, Ye JC, Yang Y, Wang XL, et al. Scr Mater 2011;64:868.
- [12] Tong CJ, Chen YL, Chen SK, Yeh JW, Shun TT, Tsau CH, et al. Metall Mater Trans A 2005;36A:881.

- [13] Tsai CW, Tsai MH, Yeh JW, Yang CC. J Alloys Compd 2010;490:160.
- [14] Tong CJ, Chen MR, Chen SK, Yeh JW, Shun TT, Lin SJ, et al. Metall Mater Trans A 2005;36A:1263.
- [15] Zhang Y, Ma SG, Qiao JW. Metall Mater Trans A 2012;43:2625.
- [16] Kuznetsov AV, Shaysultanov DG, Stepanov ND, Salishchev GA, Senkov ON. Mater Sci Eng A 2012;533:107.
- [17] Flores KM, Johnson WL, Dauskardt RH. Scr Mater 2003;49:1181.
- [18] Chuang CP, Huang JH, Dmowski W, Liaw PK, Li R, Zhang T, et al. Appl Phys Lett 2009;95:241901.
- [19] Wang GY, Liaw PK, Yokoyama Y, Inoue A, Liu CT. Mater Sci Eng A 2008;494:314.
- [20] CINDAS/USAF CRDA Handbooks Operation. Aerospace Structural Metals Handbook. West Lafayette (IN): Purdue University; 2001.
- [21] Mann YA. Fatigue of materials. Carlton (Australia): Melbourne University Press; 1967. p. 34–53.
- [22] ASM International. ASM handbook. Properties and selection: nonferrous alloys and special-purpose materials, vol. 2. Metals Park (OH): ASM International; 1990.
- [23] Singh S, Wanderka N, Murty BS, Glatzel U, Banhart J. Acta Mater 2011;59:182.
- [24] Hertzberg RW. Deformation and fracture mechanics of engineering materials. 4th ed. New York: John Wiley & Sons; 1995.
- [25] Lehmayr B, Staudacher S. Fat Fract Eng Mater Struct 2011. <http://dx.doi.org/10.1111/j.1460-2695.2011.01625.x>.
- [26] Pascual FG, Meeker WQ. Technometrics 1999;41:277.
- [27] Meeker WQ, Escobar LA. Statistical methods for reliability data. New York: Wiley; 1998.
- [28] Solomon HD, Amzallag C. In: Allen TR, King PJ, Nelson L, editors. Proceedings from the 12th international conference on environmental degradation of materials in nuclear power systems. Warrendale (PA): TMS; 2005. p. 1091.
- [29] Sakai T, Sakai T, Okada K, Furuichi M, Nishikawa I, Sugeta A. Int J Fatigue 2006;28:1486.
- [30] Wang QG, Apelian D, Lados DA. J Light Met 2001;1:73.
- [31] Zhang Y, Sakai T, Mori K. J Solid Mech Mater Eng 2011;4:138.
- [32] Harlow DG, Liaw PK, Peter WH, Wang G, Buchanan RA. Acta Mater 2008;56:3306.
- [33] Harlow DG. Acta Mater 2011;59:5048.
- [34] Mann N, Schafer R, Singpurwalla N. Methods for statistical analysis of reliability and life data. New York: Wiley; 1974.